



**HAL**  
open science

## Collisional Excitation and Non-LTE Modeling of Interstellar Chiral Propylene Oxide

Karlis Dzenis, A Faure, B. A. Mcguire, A. J. Remijan, P. J. Dagdigian, C.  
Rist, R. Dawes, E. Quintas-Sanchez, François Lique, M. Hochlaf

► **To cite this version:**

Karlis Dzenis, A Faure, B. A. Mcguire, A. J. Remijan, P. J. Dagdigian, et al.. Collisional Excitation and Non-LTE Modeling of Interstellar Chiral Propylene Oxide. *The Astrophysical Journal*, 2022, 926 (1), 10.3847/1538-4357/ac43b5 . hal-03592648v2

**HAL Id: hal-03592648**

**<https://hal.science/hal-03592648v2>**

Submitted on 1 Mar 2022

**HAL** is a multi-disciplinary open access archive for the deposit and dissemination of scientific research documents, whether they are published or not. The documents may come from teaching and research institutions in France or abroad, or from public or private research centers.

L'archive ouverte pluridisciplinaire **HAL**, est destinée au dépôt et à la diffusion de documents scientifiques de niveau recherche, publiés ou non, émanant des établissements d'enseignement et de recherche français ou étrangers, des laboratoires publics ou privés.



Distributed under a Creative Commons Attribution 4.0 International License



# Collisional Excitation and Non-LTE Modeling of Interstellar Chiral Propylene Oxide

Karlis Dzenis<sup>1,2,3</sup> , Alexandre Faure<sup>2</sup> , B. A. McGuire<sup>4,5</sup> , A. J. Remijan<sup>5</sup> , P. J. Dagdigan<sup>6</sup> , C. Rist<sup>2</sup>, R. Dawes<sup>7</sup>,  
E. Quintas-Sánchez<sup>7</sup>, F. Lique<sup>8</sup> , and M. Hochlaf<sup>9</sup>

<sup>1</sup> University of Edinburgh, School of Chemistry, Edinburgh EH9 3FJ, UK

<sup>2</sup> Université Grenoble Alpes, CNRS, IPAG, F-38000 Grenoble, France

<sup>3</sup> Université Grenoble Alpes, Département de Chimie Moléculaire, F-38000 Grenoble, France

<sup>4</sup> Department of Chemistry, Massachusetts Institute of Technology, Cambridge, MA 02139, USA

<sup>5</sup> National Radio Astronomy Observatory, 520 Edgemont Rd., Charlottesville, VA 22903, USA

<sup>6</sup> Department of Chemistry, The Johns Hopkins University, Baltimore, MD 21218-2685, USA

<sup>7</sup> Department of Chemistry, Missouri University of Science and Technology, Rolla, Missouri 65409, USA

<sup>8</sup> Université du Rennes, CNRS, IPR (Institut de Physique de Rennes)UMR 6251, F-35000 Rennes, France

<sup>9</sup> Université Gustave Eiffel, COSYS/LISIS, 5 Bd Descartes, F-77454, Champs sur Marne, France; [alexandre.faure@univ-grenoble-alpes.fr](mailto:alexandre.faure@univ-grenoble-alpes.fr)

Received 2021 September 14; revised 2021 December 6; accepted 2021 December 14; published 2022 February 8

## Abstract

The first set of theoretical rotational cross sections for propylene oxide (CH<sub>3</sub>CHCH<sub>2</sub>O) colliding with cold He atoms has been obtained at the full quantum level using a high-accuracy potential energy surface. By scaling the collision reduced mass, rotational rate coefficients for collisions with para-H<sub>2</sub> are deduced in the temperature range 5–30 K. These collisional coefficients are combined with radiative data in a non-LTE radiative transfer model in order to reproduce observations of propylene oxide made toward the Sagittarius B2(N) molecular cloud with the Green Bank and Parkes radio telescopes. The three detected absorption lines are found to probe the cold ( $\sim 10$  K) and translucent ( $n_{\text{H}} \sim 2000 \text{ cm}^{-3}$ ) gas in the outer edges of the extended Sgr B2(N) envelope. The derived column density for propylene oxide is  $N_{\text{tot}} \sim 3 \times 10^{12} \text{ cm}^{-2}$ , corresponding to a fractional abundance relative to total hydrogen of  $\sim 2.5 \times 10^{-11}$ . The present results are expected to help our understanding of the chemistry of propylene oxide, including a potential enantiomeric excess, in the cold interstellar medium.

*Unified Astronomy Thesaurus concepts:* [Astrochemistry \(75\)](#); [Chemical abundances \(224\)](#); [Interstellar abundances \(832\)](#)

## 1. Introduction

Molecular chirality was discovered in 1848 by the French chemist Louis Pasteur, but the term chirality was only introduced in 1894 by Lord Kelvin (Gal 2011). It was defined by Vladimir Prelog in his 1975 Nobel lecture:<sup>10</sup> “An object is chiral if it cannot be brought into congruence with its mirror image by translation and rotation.” Chiral molecules are components of essential building blocks of all life on Earth, specifically nucleic acids and proteins. They can exist as dextrorotatory (D) or levorotatory (L) enantiomers depending on the way they rotate plane-polarized light, clockwise or counterclockwise, respectively. Interestingly, life on Earth is exclusively homochiral because nucleic acids contain only D-sugars while proteins are built from L-amino acid monomers. While homochirality is seen as a requirement for the evolution of life (Joyce et al. 1987), its origins are still unclear and are actively discussed. Several studies suggest that the origin of a primordial enantiomeric excess (*ee*) is in fact extraterrestrial (Bailey et al. 1998). This is consistent with evidence from laboratory measurements of *ee* of the L enantiomer of several amino acids that were found in Murchison and Orgueil meteorite samples that are the oldest samples with a measured *ee* (Glavin & Dworkin 2009).

A number of astronomically relevant mechanisms that could produce a primordial *ee* have been proposed in the literature. A small imbalance in chiral symmetry has been demonstrated experimentally to arise in gas-phase by radiolysis with beta-decay electrons (Dreiling & Gay 2014). Alternatively, homochirality can be produced through asymmetric photochemistry of molecules by circularly polarized light (Modica et al. 2014). Overall, these clues suggest a scenario where an enantiomeric enrichment of chiral organic molecules was produced in molecular clouds of the interstellar medium (ISM), which in subsequent solar life cycle stages was incorporated in the formation of a circumstellar disk, new planets, meteorites, or comets. Eventually the (amplified) enantiomerically enriched organic material would have been delivered to Earth and influenced the evolution of prebiotic organic molecules.

The prospect of this scenario has motivated further investigations aimed at detecting signatures of chiral molecules outside the Earth and our solar system. To date, more than 250 molecules have been detected in the ISM, about a third of which are complex organic molecules (COMs; Herbst & van Dishoeck 2009), yet only one, propylene oxide (CH<sub>3</sub>CHCH<sub>2</sub>O), is a chiral molecule. Propylene oxide was detected in 2016 toward the center of the Milky Way galaxy, in cold, presumably low-density gas of the high-mass star-forming region Sagittarius B2(N) (McGuire et al. 2016). With these observations, it was not possible to distinguish between the enantiomers of propylene oxide and determine if an *ee* exists. Recently, however, a Gas Chromatographic–Mass Spectroscopic (GC-MS) analysis of ethanol extracts of Murchison meteorite samples reported the presence of two chiral derivatives of propylene oxide with an *ee* averaging to

<sup>10</sup> <https://www.nobelprize.org/uploads/2018/06/prelog-lecture.pdf>

$\sim 10\%$  (Pizzarello & Yarnes 2018). The measured  $ee$  from meteorite samples cannot be related to the composition of propylene oxide detected in the ISM from this study alone. Therefore, two questions remain unanswered: Does an  $ee$  of propylene oxide exist in the ISM? If it does, how was it produced? To determine if an  $ee$  of propylene oxide can exist in the ISM, it is important to understand formation pathways to this molecule, which could then be evaluated in astrochemical models if the abundance is known. Recent experimental works have shown that propylene oxide can be synthesized in interstellar ice analogs under irradiation with MeV protons (Hudson et al. 2017) or keV electrons (Bergantini et al. 2018). But other non-energetic mechanisms, including gas-phase synthesis (Bodo et al. 2019), may exist.

To elucidate the possible formation pathways, however, it is first crucial to determine an accurate column density and abundance of propylene oxide, which constitutes the main aim of this study. Initial estimates of propylene oxide abundance toward the envelope of Sgr B2 have been made by Cunningham et al. (2007), who determined an upper limit for propylene oxide column density in the Sgr B2 Large Molecule Heimat (N-LMH) compact source at  $6.7 \times 10^{14} \text{ cm}^{-2}$  with a high excitation temperature,  $T_{\text{ex}} = 200 \text{ K}$ . McGuire et al. (2016) identified propylene oxide by three rotational transitions in absorption toward Sgr B2(N), and their observations were fitted the best for an excitation temperature  $T_{\text{ex}} = 5.2 \text{ K}$  and a column density of  $1 \times 10^{13} \text{ cm}^{-2}$ , which was consistent with the previously set upper boundary. In the analysis of McGuire et al. (2016), it was noted that the excitation temperature that fits their observations best was not well-constrained and other column densities for an excitation temperature range  $5 \text{ K} \leq T_{\text{ex}} \leq 35 \text{ K}$  could also produce a good fit. This was highlighted by some of us (Faure et al. 2019) as a source of uncertainty in the derived abundance. Additionally, the rotational level populations of propylene oxide cannot be accurately described by a single excitation temperature, as it relies on the local thermodynamic equilibrium (LTE) assumption in which the detected levels follow a Boltzmann distribution. In general, LTE conditions are not fulfilled, due to the low density of ISM environments, including the envelope of Sgr B2(N) (Faure et al. 2014). Instead, a non-LTE approach is necessary to provide accurate column densities and also to extract the local physical conditions (density and kinetic temperature).

In 2019, some of us generated the 3D potential energy surface (PES) of the  $\text{CH}_3\text{CHCH}_2\text{O}-\text{He}$  interacting system (Faure et al. 2019). The first objective of this study is to use this PES to calculate rotational cross sections for the inelastic collision between propylene oxide and He at low collision energy and at the quantum level. Using standard reduced-mass scaling, rate coefficients for propylene oxide interacting with para- $\text{H}_2$ , the most abundant collider in the cold ISM, are then deduced for kinetic temperatures below 30 K. The second objective is to combine collisional and radiative rates in a non-LTE model in order to reproduce the detected rotational lines of propylene oxide by McGuire et al. (2016) and to determine both an accurate column density for propylene oxide and the physical conditions in the absorbing cold shell toward Sgr B2(N).

Section 2 is dedicated to rotational cross-section calculations, which are used to determine rotational (de)excitation rate coefficients. Radiative transfer calculations are described in

Section 3. Conclusions and future work are discussed in Section 4.

## 2. Collisional Cross Sections and Rate Coefficients

Quantum scattering calculations are based on a high-accuracy  $\text{CH}_3\text{CHCH}_2\text{O}-\text{He}$  PES that was previously computed, characterized and presented by Faure et al. (2019). Briefly, this PES was determined using the explicitly correlated coupled-cluster theory extended to the basis set limit [CCSD (T)-F12b/CBS] and it was accurately fitted to spherical harmonics. The global minimum of the fitted PES was found at  $-79.5 \text{ cm}^{-1}$  relative to the energy of separated molecules. We note that this value is in very good agreement (within  $1 \text{ cm}^{-1}$ ) with the global minimum of the  $\text{CH}_3\text{CHCH}_2\text{O}-\text{He}$  PES built from the analysis of experimental scattering data Palazzetti et al. (2021). In the study of Faure et al. (2019), rotational cross sections were computed for a single collision energy of  $10 \text{ cm}^{-1}$ . Here, we have extended the calculations to cover an extensive grid of total energies ( $0.5-213 \text{ cm}^{-1}$ ) and then derive rate coefficients in the temperature range 5–30 K. Because we are only concerned with energy transfer between helium and randomly oriented propylene oxide, chiral effects are entirely ignored.

Cross-section calculations presented below employed three assumptions. First, it was assumed that cross sections for propylene oxide colliding with para- $\text{H}_2$  are equal to those with He. This assumption should be appropriate for molecules with more than three heavy atoms if the collision partner is para- $\text{H}_2$  in its ground rotational state ( $j=0$ ) as found for collisional excitation of  $\text{HC}_3\text{N}$  by He, ortho- $\text{H}_2$ , and para- $\text{H}_2$  (Wernli et al. 2007a, 2007b). The population of ortho- $\text{H}_2$  can be considered insignificant compared to para- $\text{H}_2$  below 30 K (Faure et al. 2013). Second, propylene oxide was treated as a rigid rotor. This approximation is justified for scattering calculations at low collision energy, as demonstrated by Faure et al. (2016) for the  $\text{CO}-\text{H}_2$  system. Third, due to internal rotation (methyl torsion), rotational levels of propylene oxide are split by tunneling into doublets, the nondegenerate  $A$  levels, and the doubly degenerate  $E$  levels (Herschbach & Swalen 1958). In the ground torsional state, however, the splitting could not be resolved in the astronomical observations because the barrier to internal rotation is very high (Stahl et al. 2021). As a result, we used a single rigid-rotor asymmetric top Hamiltonian with experimental ground-state rotational constants  $A = 0.6012 \text{ cm}^{-1}$ ,  $B = 0.2229 \text{ cm}^{-1}$ , and  $C = 0.1985 \text{ cm}^{-1}$  taken from the Cologne Database for Molecular Spectroscopy (CDMS; Müller et al. 2005).

Cross-section calculations were performed using the Hibridon code (Alexander et al. 2021), which is based on solving the time-independent close-coupling (CC) equations. The general theory for quantum scattering calculations within the CC formalism, introduced by Garrison et al. (1976) for an asymmetric rotor colliding with a structureless atom, was extended to molecules like propylene oxide that do not possess any symmetry elements by Faure et al. (2019) and was applied here. The second-order differential CC equations were integrated using the hybrid propagator of Alexander & Manolopoulos (1987) with propagation parameters as in Faure et al. (2019). Cross sections for purely rotational transitions were calculated for a total energy range below the first torsional mode of propylene oxide at  $213 \text{ cm}^{-1}$  (Šebestík & Bouř 2011), with an energy step of  $0.5 \text{ cm}^{-1}$  below  $E_{\text{tot}} = 80 \text{ cm}^{-1}$  to

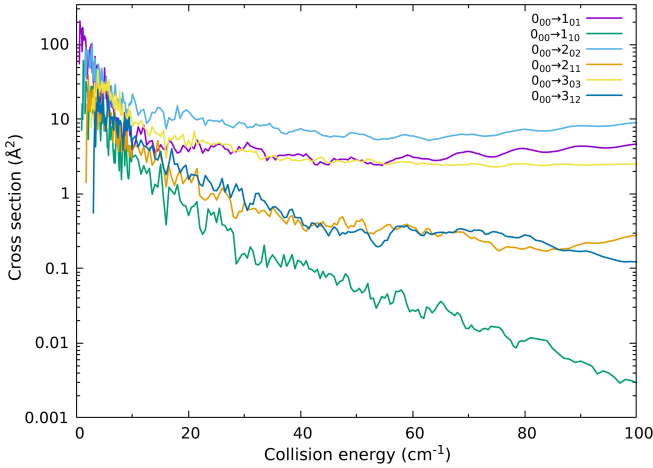


**Figure 1.** Integral cross sections for state-to-state rotational excitation of propylene oxide from the rotational ground state ( $0_{00}$ ) by collisions with He.

account for the numerous resonances arising from quantum effects. The rotational constants of propylene oxide, as listed above, are moderately small and the rotational spectrum relatively dense; therefore, solving CC equations was expected to be computationally demanding with respect to CPU time and memory.

The rotational states are defined as  $j_{K_a K_c}$ , where  $j$  is the angular momentum quantum number, and  $K_a$  and  $K_c$  are projections of  $j$  along the  $a$  and  $c$  axes, which by convention are the axes with the smallest and largest moments of inertia, respectively. A basis of internal states with  $j_{\max} = 22$  was selected to ensure that inelastic cross sections for all transitions among the lowest 100 rotational levels (up to  $11_{29}$  at  $29.862 \text{ cm}^{-1}$ ) were converged to within 20%. As discussed in Faure et al. (2019), the convergence of cross-section calculations was found to be slow due to couplings to many energetically inaccessible rotational states (closed channels). To limit the computational expenses while maintaining accuracy, two additional parameters, threshold rotational energy ( $E_{\max}$ ) and total angular momentum ( $J$ ), were optimized in the total energy range to reach a global convergence of total cross sections (summed over  $J$ ) better than 20%. This was achieved with  $E_{\max} = 160\text{--}213 \text{ cm}^{-1}$  and for partial waves  $J \leq 50$ . The largest calculations involved more than 7300 coupled channels and about 30 CPU hours for one partial wave on Intel Gold processors. A total of  $\sim 2 \times 10^5$  CPU hours were consumed for the whole project.

Integral cross sections for excitations from the ground state to rotational levels that are relevant to the observed absorption lines (i.e.,  $1_{01}$ ,  $1_{10}$ ,  $2_{02}$ ,  $2_{11}$ ,  $3_{03}$ , and  $3_{12}$ ) are presented as a function of collision energy ( $E_{\text{col}}$ ) in Figure 1.

In general, the calculated cross sections are highest at low collision energies with many resonances that contribute to the peak-trough pattern and decrease with increasing collision energies until reaching a plateau. As expected, the cross sections at  $10 \text{ cm}^{-1}$  are in excellent agreement with those of Faure et al. (2019).

Rate coefficients  $k(T)$  for each collisional transition ( $j_{K_a K_c} \rightarrow j'_{K'_a K'_c}$ ) were calculated in the temperature range  $T_{\text{kin}} = 5\text{--}30 \text{ K}$  by integrating the total cross sections ( $\sigma$ ) over a Maxwell–Boltzmann distribution of velocities, which are directly related to the collision (kinetic) energy ( $E_{\text{col}}$ ) according

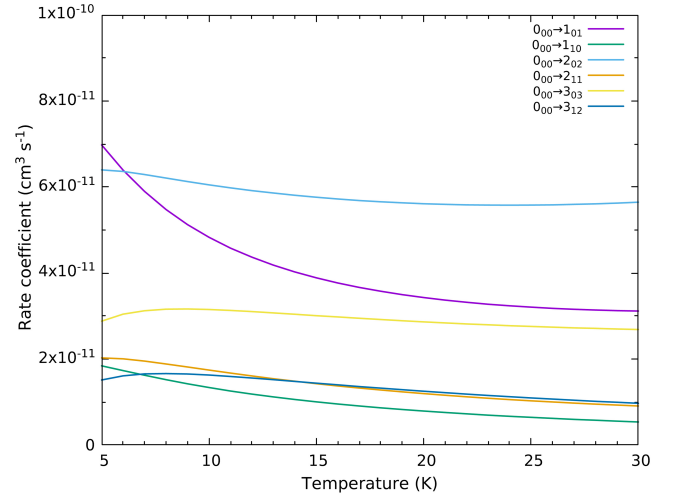


**Figure 2.** Rate coefficients for rotational excitation of propylene oxide from the rotational ground state ( $0_{00}$ ) by para- $\text{H}_2$ .

to Equation (1):

$$k(T_{\text{kin}}) = \sqrt{\frac{8k_B T_{\text{kin}}}{\pi\mu}} \int_0^\infty \sigma(x) x \exp(-x) dx, \quad (1)$$

where  $x = E_{\text{col}}/(k_B T_{\text{kin}})$ ,  $k_B$  is the Boltzmann constant, and  $\mu$  is the collisional reduced mass. Using the aforementioned assumption that cross sections for collisions with He are equal to those with para- $\text{H}_2$ , the reduced mass of propylene oxide and  $\text{H}_2$  ( $\mu = 1.94800083 \text{ amu}$ ) was used. Rate coefficients are displayed as a function of temperature for excitation from the ground state to rotational levels relevant to the observed absorption lines (i.e.,  $1_{01}$ ,  $1_{10}$ ,  $2_{02}$ ,  $2_{11}$ ,  $3_{03}$ , and  $3_{12}$ ) in Figure 2. Rate coefficients clearly follow the ordering of cross sections in Figure 1, due to their relation through Equation (1). However, their dependence on temperature is smooth compared to the pattern of cross sections, which is a result of the Maxwell–Boltzmann averaging. The favored transition with the largest rate coefficient is  $0_{00} \rightarrow 2_{02}$ , which corresponds to a propensity rule  $\Delta j = 2$  and  $\Delta K_a = 0$ , while the next two highest rate coefficients are observed for transitions  $0_{00} \rightarrow 1_{01}$  and  $0_{00} \rightarrow 3_{03}$ , respectively. This trend indicates the conservation of the angular momentum along the axis of smallest moment of inertia ( $a$  axis), since  $\Delta K_a = 0$ . Interestingly, such ordering of collisional rate coefficients for transitions from the ground state corroborates the detection of rotational transitions of propylene oxide (i.e.,  $1_{01} \rightarrow 1_{10}$ ,  $2_{02} \rightarrow 2_{11}$ , and  $3_{03} \rightarrow 3_{12}$ ) in absorption. Nevertheless, the real populations of rotational levels can only be determined by considering also the radiative processes in a non-LTE model for specific physical conditions.

### 3. Non-LTE Modeling

The non-LTE radiative transfer calculations were performed with Radex (van der Tak et al. 2007) using the escape probability approximation for a uniform sphere. The model incorporated both the calculated collisional rate coefficients among the 100 lowest rotational levels (a total of 4950 de-excitation transitions) and Einstein coefficients for radiative transitions obtained from the CDMS database (Müller et al. 2005). The only ambient radiation field assumed is the cosmic

microwave background (CMB), and we omitted, in particular, the diluted infrared emission from the hot cores Sgr B2(M) and Sgr B2(N), as well as the extended microwave continuum from the Galactic Center region. These neglected sources of radiative pumping (absorption and stimulated emission) can possibly compete with collisional processes, and they will be investigated in future works. The Radex code was applied to calculate the excitation temperature ( $T_{\text{ex}}$ ) and opacity ( $\tau$ ) of each transition at physical conditions specified by a kinetic temperature ( $T_{\text{kin}}$ ), density of  $\text{H}_2$  ( $n(\text{H}_2)$ ) and column density of propylene oxide ( $N_{\text{tot}}$ ). A range for each physical parameter was selected to compute a grid of non-LTE models; in particular,  $T_{\text{kin}}$  was constrained to 5–30 K,  $n(\text{H}_2)$  was restricted to  $10\text{--}10^6\text{ cm}^{-3}$ , and  $N_{\text{tot}}$  was restricted to  $10^{12}\text{--}10^{14}\text{ cm}^{-2}$ . A linewidth, full width at half maximum (FWHM) of  $13\text{ km s}^{-1}$  was used as determined by McGuire et al. (2016).

For each transition, a measurable line intensity at a frequency  $\nu$ , (corrected) antenna temperature  $T_a^*$  (in Kelvin), can be expressed in terms of  $T_{\text{ex}}$  and  $\tau$  as follows:

$$T_a^*(\nu) = (\eta_b B J_\nu(T_{\text{ex}}) - \eta_b B J_\nu(T_{\text{cmb}}) - T_c(\nu))(1 - \exp(-\tau)), \quad (2)$$

where the Green Bank Telescope (GBT) beam efficiency  $\eta_b$  and the main beam continuum temperature  $T_c(\nu) = 10^{-1.06 \log_{10}(\nu[\text{GHz}]) + 2.3}$  were taken from Hollis et al. (2007),  $J_\nu(T) = (h\nu/k_B)/(e^{h\nu/k_B T} - 1)$ ,  $T_{\text{cmb}}$  is the CMB temperature (2.73 K), and  $B$  is the GBT beam dilution factor accounting for the spatial overlap of the Sgr B2(N) continuum with the GBT beam (both assumed to have a Gaussian shape),  $B = \theta_s^2/(\theta_s^2 + \theta_b^2)$ , with  $\theta_s$  and  $\theta_b$  as the source and beam sizes, respectively. The size of the background continuum source against which propylene oxide absorbs was taken as  $\theta_s = 20''$ , as in McGuire et al. (2016). We note that this value is consistent with  $\theta_s = 77''(\nu)^{-0.52}$ , as derived by Hollis et al. (2007; for the north component) when  $\nu \sim 12\text{--}14\text{ GHz}$ . The GBT half-power beamwidth was taken as  $\theta_b = 754''/\nu$ , where  $\nu$  is in units of GHz.

Importantly, only transitions  $2_{02} \rightarrow 2_{11}$  and  $3_{03} \rightarrow 3_{12}$  were detected by GBT, while transition  $1_{01} \rightarrow 1_{10}$  was detected with a beam almost twice the size of GBT by the Parkes Radio Telescope and incorporated a contribution to the continuum background from an adjacent source, Sgr B2(M). Therefore, in our quantitative model we focus on the two lines observed by GBT, namely  $2_{02} \rightarrow 2_{11}$  and  $3_{03} \rightarrow 3_{12}$ , and we neglect the contribution of sources other than Sgr B2(N). Thus, the observed intensity of the Parkes line cannot be compared to our predictions.

Physical parameters that best model the observed  $T_a^*$  of the two absorption lines detected by GBT were determined using a least-squares fit. The Parkes line was also employed and restricted to be in absorption, i.e., with negative  $T_a^*$  values. The best-fit non-LTE model is compared to the two observed GBT absorption line intensities in Figure 3. We note that a local standard of rest velocity ( $V_{\text{LSR}}$ ) of  $+64\text{ km.s}^{-1}$ , characteristic of the extended envelope of Sgr B2(N), was assumed for the detected lines. Other details about GBT and Parkes observations can be found in McGuire et al. (2016). Additionally, we present in the middle panel of Figure 3 an LTE model where all lines are constrained to have the same excitation temperature.

In our LTE model, the density was taken as  $n(\text{H}_2) = 1 \times 10^{10}\text{ cm}^{-3}$  in order to guarantee LTE populations.

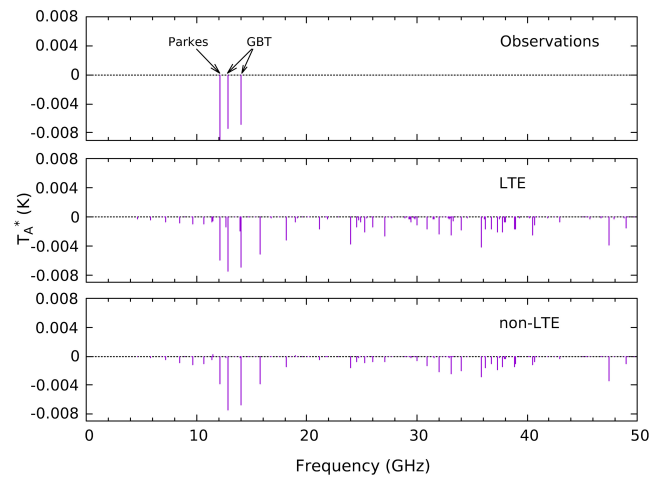


**Figure 3.** Observed (top), modeled LTE (middle), and non-LTE (bottom) line intensities ( $T_a^*$ ) of rotational transitions of propylene oxide in the frequency range of 1–50 GHz.

Indeed, the critical densities<sup>11</sup> for the detected levels  $1_{01}$ ,  $2_{02}$ , and  $3_{03}$  are  $\sim 10^3\text{ cm}^{-3}$ . The excitation temperature  $T_{\text{ex}} = T_{\text{kin}} = 5.2\text{ K}$  and column density  $N_{\text{tot}} = 9 \times 10^{12}\text{ cm}^{-2}$  predicts the observed GBT line intensities closely (within 0.1 mK), aligning well with LTE modeling results by McGuire et al. (2016), who found the best fit with the same  $T_{\text{ex}}$  and  $N_{\text{tot}} = 1 \times 10^{13}\text{ cm}^{-2}$ .

The non-LTE calculations provide the best fit to the GBT line intensities for model parameters  $n(\text{H}_2) = 1000\text{ cm}^{-3}$ ,  $T_{\text{kin}} = 8\text{ K}$ , and  $N_{\text{tot}} = 3 \times 10^{12}\text{ cm}^{-2}$ . The resulting root-mean-square (rms) error is very low ( $< 0.1\text{ mK}$ ), as expected for an overfit model. Exploring the 3D grid of  $\chi^2$  values shows that the kinetic temperature and  $\text{H}_2$  density are poorly constrained while the best-fit value for the propylene oxide column density corresponds to a steep minimum. It should be noted that our best-fit model is also consistent with the nondetection of other rotational lines above the continuum noise by previous surveys in the range 0–120 GHz (Cunningham et al. 2007; McGuire et al. 2016). In particular, we report in Table 1 the non-LTE predicted intensity for the strongest transitions ( $> 1.5\text{ mK}$ ) in the range 1–50 GHz alongside their opacity, excitation temperature, and the noise level of the PRIMOS observations or the cause of a nondetection (e.g., missing data, or radio frequency interference (RFI)).<sup>12</sup>

In Figure 3, both LTE and non-LTE spectra display a potential signature of propylene oxide at 15.8 GHz in absorption with similar intensities of  $-5.5\text{ mK}$  and  $-3.8\text{ mK}$ , respectively. This line is  $\sim 1.8$  times weaker than the faintest detected transition  $3_{03} \rightarrow 3_{12}$  at 14.0 GHz and corresponds to the transition  $4_{04} \rightarrow 4_{13}$ , which was not detected with the GBT or Parkes telescope, due to absence of a corresponding receiver (McGuire et al. 2016). More generally, we note that, although the derived column density is a factor of three larger, the LTE spectrum agrees surprisingly well with the non-LTE spectrum. This can be explained by similar opacities (in the range  $2.7\text{--}5.8 \times 10^{-4}$ ) and excitation temperatures (in the range 2.6–5.2 K) for the three detected lines, which both contribute to

<sup>11</sup> The critical density for a particular level is given by the ratio between the sum of all radiative rates and the sum of all de-excitation collisional rates from this level.

<sup>12</sup> Data are available from the NRAO archive at <https://archive.nrao.edu> under GBT project code AGBT07A\_051.

**Table 1**  
Predicted Intensity for the Strongest Transitions of Propylene Oxide

$\nu$ (GHz)	$\tau$	$T_{\text{ex}}$ (K)	$T_a^*$ (K)	Noise level (K)
12.0724	$2.734 \times 10^{-4}$	4.09	-0.0039	RFI
12.8373	$5.580 \times 10^{-4}$	2.74	-0.0074	Detected Feature
14.0478	$5.556 \times 10^{-4}$	2.61	-0.0067	Detected Feature
15.7751	$3.542 \times 10^{-4}$	2.89	-0.0038	No Data
18.1036	$1.651 \times 10^{-4}$	3.38	-0.0015	0.0035
23.9752	$2.586 \times 10^{-4}$	5.81	-0.0016	0.0053
32.0418	$3.965 \times 10^{-4}$	2.15	-0.0021	0.0229
33.1211	$5.021 \times 10^{-4}$	2.25	-0.0025	0.0075
34.0591	$4.055 \times 10^{-4}$	2.45	-0.0020	0.0075
35.8779	$7.083 \times 10^{-4}$	4.11	-0.0029	0.0074
36.2171	$3.639 \times 10^{-4}$	2.65	-0.0016	0.0100
37.3340	$4.361 \times 10^{-4}$	2.50	-0.0019	0.0104
47.4285	$1.105 \times 10^{-3}$	3.52	-0.0034	0.0085

**Note.** The table lists the opacity, excitation temperature and intensity of the (13) strongest absorption lines in our best-fit non-LTE model below 50 GHz, along with the noise level of the PRIMOS observations.

$T_a^*$ . Still, some lines are predicted to be inverted (i.e., with negative  $T_{\text{ex}}$ ) with the non-LTE model, although none of these potential weak masers have sufficient opacities to become detectable in this source.

The uncertainty in the three model parameters ( $T_{\text{kin}}$ ,  $n(\text{H}_2)$  and  $N_{\text{tot}}$ ) is difficult to assess statistically with only three detected lines. Assuming the main source of uncertainty is introduced by the measurements as reported by McGuire et al. (2016), we have considered the  $1\sigma$  deviation limits for the intensities of transitions  $2_{02} \rightarrow 2_{11}$  ( $\pm 5$  mK) and  $3_{03} \rightarrow 3_{12}$  ( $\pm 6$  mK) and the corresponding interval in the three physical parameters. The best-fit models at the  $1\sigma$  limits of line intensities constrain the kinetic temperature to the range  $T_{\text{kin}} = 5\text{--}13$  K, the  $\text{H}_2$  density to the range  $n(\text{H}_2) = 800\text{--}1900$   $\text{cm}^{-3}$ , and the column density to the range  $N_{\text{tot}} = 3 \times 10^{12}\text{--}4 \times 10^{12}$   $\text{cm}^{-2}$ . We cannot, however, exclude kinetic temperatures larger than 13-K:  $T_{\text{kin}}$  in the range 20–30-K also provide reasonable results, but with larger rms error.

It is useful to analyze the excitation temperatures  $T_{\text{ex}}$  and opacities  $\tau$  of all three detected transitions.  $T_{\text{ex}}$  and  $\tau$  are displayed as a function of  $n(\text{H}_2)$  in Figures 4 and 5 for the best-fit non-LTE model with parameters  $T_{\text{kin}} = 8$  K and  $N_{\text{tot}} = 3 \times 10^{12}$   $\text{cm}^{-2}$ . For all three transitions,  $T_{\text{ex}}$  and  $\tau$  are positive, except in the range  $3 \times 10^3$   $\text{cm}^{-3} \lesssim n(\text{H}_2) \lesssim 3 \times 10^4$   $\text{cm}^{-3}$ , where the Parkes line at 12.1 GHz gets inverted and the molecule is capable of masing (opacity is, however, very low). When  $n(\text{H}_2) \gtrsim 3 \times 10^4$   $\text{cm}^{-3}$ , all opacities are positive and small, while  $T_{\text{ex}}$  gets closer to  $T_{\text{kin}}$  as the system approaches LTE. Since all three lines were detected in absorption, only the range of  $n(\text{H}_2)$  where  $T_{\text{ex}}$  and  $\tau$  are positive for all transitions can be considered. The opacity further constrains the  $\text{H}_2$  volume density, as in the range  $n(\text{H}_2) > 3 \times 10^4$   $\text{cm}^{-3}$ , the opacities are very low ( $\sim 1 \times 10^{-5}$ ) and the absorption lines would not be detected above the continuum noise. As a result, the non-LTE calculations strongly restrict the observations of propylene oxide to a low-density region in the envelope of Sgr B2(N) with  $n(\text{H}_2) < 3 \times 10^3$   $\text{cm}^{-3}$ . At higher densities, opacities become so low that the lines would be undetectable.

Finally, we note that a non-LTE model for propylene oxide was presented recently by Das et al. (2019). In their work, the authors employed the collisional rate coefficients of  $\text{CH}_3\text{OH}$

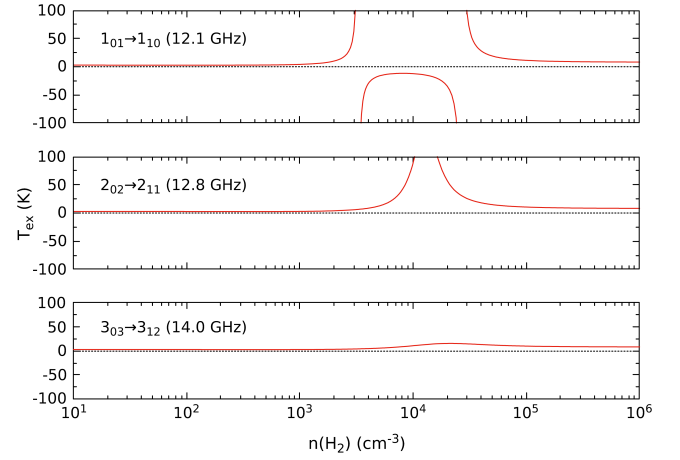


**Figure 4.** Excitation temperature as a function of  $\text{H}_2$  volume density ( $n(\text{H}_2)$ ) for the observed rotational transitions of propylene oxide toward Sgr B2 (N),  $1_{01} \rightarrow 1_{10}$  (12.1 GHz),  $2_{02} \rightarrow 2_{11}$  (12.8 GHz), and  $3_{03} \rightarrow 3_{12}$  (14.0 GHz) at  $T_{\text{kin}} = 8$  K and  $N_{\text{tot}} = 3 \times 10^{12}$   $\text{cm}^{-2}$ .

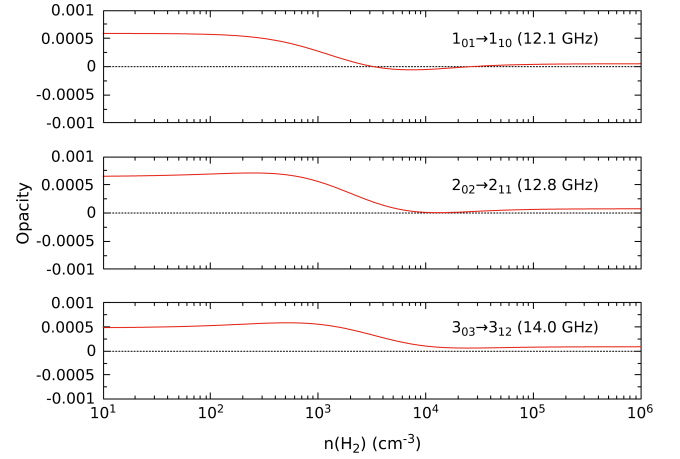


**Figure 5.** Opacity as a function of  $\text{H}_2$  volume density ( $n(\text{H}_2)$ ) for the observed rotational transitions of propylene oxide toward Sgr B2 (N),  $1_{01} \rightarrow 1_{10}$  (12.1 GHz),  $2_{02} \rightarrow 2_{11}$  (12.8 GHz), and  $3_{03} \rightarrow 3_{12}$  (14.0 GHz) at  $T_{\text{kin}} = 8$  K and  $N_{\text{tot}} = 3 \times 10^{12}$   $\text{cm}^{-2}$ .

with  $\text{H}_2$ , which is obviously a crude approximation to mimic the  $\text{CH}_3\text{CHCH}_2\text{O}\text{--}\text{H}_2$  system. Their best model was found for  $T_{\text{kin}} = 5\text{--}10$  K and  $n(\text{H}_2) > 10^4$   $\text{cm}^{-3}$ . The high densities found by these authors likely reflect the approximate collisional data, as well as the propylene oxide column density kept constant at  $1 \times 10^{13}$   $\text{cm}^{-2}$ .

#### 4. Discussion

The presented non-LTE calculations suggest that propylene oxide was detected toward a cold,  $T_{\text{kin}} \sim 10$  K, and moderately dense  $n(\text{H}_2) \sim 1000$   $\text{cm}^{-3}$  region toward Sgr B2(N) with a column density  $N_{\text{tot}} \sim 3 \times 10^{12}$   $\text{cm}^{-2}$ . The determined column density of propylene oxide was found to be robust and it is also in relative good agreement with previous estimates: it is a factor of  $\sim 3$  lower than the LTE value estimated by McGuire et al. (2016), and as expected, is below the upper limit at  $6.7 \times 10^{14}$   $\text{cm}^{-2}$  set by Cunningham et al. (2007). The density, and in particular the kinetic temperature, are less well determined. They are still consistent with detection of other COMs toward the extended cold envelope of Sgr B2(N), with

low and subthermal rotational temperatures ( $<10$  K; see Corby et al. (2015) and references therein).

The derived physical parameters are characteristic of *translucent* regions, which are not commonly associated with the presence or chemistry of COMs due to the presence of the (only partially shielded) UV interstellar radiation field that contributes to dissociation of large molecules. The formation of COMs is typically thought to occur in more dense and shielded regions, like cold prestellar cores and hot cores, where the proton density ( $n_{\text{H}} = 2n(\text{H}_2)$ ) is larger than  $\sim 10^5 \text{ cm}^{-3}$  (Bacmann et al. 2012). But COMs have been also detected in UV-irradiated, photon-dominated regions (Gratier et al. 2013). Toward the envelope of Sgr B2(N), the series of  $\text{HCOOCH}_3$  weak maser lines below 30 GHz were found to be associated with lower densities  $n_{\text{H}} \sim 3 \times 10^4 \text{ cm}^{-3}$  (Faure et al. 2014). Here, the derived density is an order of magnitude lower and may be associated with the outer edges of the extended Sgr B2 (N) envelope. Our results therefore question the chemistry and formation of complex molecules in translucent conditions. This is not a unique result, as recent analysis of (GBT) PRIMOS and Atacama Large Millimeter/submillimeter Array (ALMA) EMOCA survey data also identified several COMs in translucent clouds along the line of sight to Sgr B2(N) (Corby 2016; Thiel et al. 2017, 2019). We note in this context the very recent work by Wang et al. (2021) on the chemistry of COMs in the extended region of Sgr B2, where the authors emphasize the possible role of X-ray flares on the reactive desorption process.

Indeed, the detection of gas-phase COMs at temperatures well below the thermal desorption temperature has been noted in a variety of environments in the last several years. These include species like  $\text{CH}_2\text{OHCHO}$ ,  $\text{CH}_3\text{CHO}$ ,  $\text{CH}_2\text{CHCHO}$ ,  $\text{CH}_3\text{CH}_2\text{CHO}$ , and  $\text{CNCHO}$ , all first detected toward Sgr B2 (see Remijan et al. 2008, and references therein). Requena-Torres et al. (2006) conducted an extensive survey of complex molecules in the Galactic center, noting a number of species with substantially subthermal excitation temperatures. One of these sources, G+0.693-0.027, has seen substantial recent interest with ALMA observations, resulting in a number of detections of new organic species, all well below the kinetic temperature (see, e.g., Rivilla et al. 2020). Perhaps even more striking are the observations of COMs in the cold, dark, starless core TMC-1 (see, e.g., Agúndez et al. 2021), where the kinetic temperatures are well-known to be substantially below the thermal desorption threshold. A number of physical and physiochemical processes have been theorized to account for the nonthermal desorption of COMs from grain surfaces (Paulive et al. 2021), as well as substantial quantum chemical efforts suggesting potential new pathways for gas-phase formation (Balucani et al. 2018). A generalized picture of these processes, and under what conditions they dominate, remains absent. The detection and quantification of more COMs under subthermal conditions, especially using non-LTE methods that provide insight into the kinetic temperature and density conditions, is clearly needed.

Another interesting constraint is provided by the detection of acetone and propanal, two structural isomers of propylene oxide, also observed in absorption toward Sgr B2(N) by McGuire et al. (2016). Excitation temperatures of 6.2 K were determined, suggesting similar excitation conditions, with column densities of  $2.1 \times 10^{14} \text{ cm}^{-2}$  for acetone and  $6 \times 10^{13} \text{ cm}^{-2}$  for propanal (McGuire et al. 2016). While the

relative column densities of the three  $\text{C}_3\text{H}_6\text{O}$  isomers follow thermodynamics, their similar values in such a cold environment indicates a strongly nonequilibrium and kinetically controlled chemistry (propylene oxide is less stable than propanal by about 13,000 K; see Bergantini et al. 2018).

Finally, we can try to estimate the abundance, relative to the total hydrogen density, of propylene oxide in the outer shell of the Sgr B2(N) envelope. Assuming the low-density layer in front of Sgr B2(N), where  $n(\text{H}_2) = 1000 \text{ cm}^{-3}$ , extends over  $\sim 19$  pc, as described in Schmiedeke et al. (2016), the foreground  $\text{H}_2$  column density is  $\sim 6 \times 10^{22} \text{ cm}^{-2}$  and the fractional abundance of propylene oxide is  $\sim 2.5 \times 10^{-11}$ . This is likely a lower limit, since the actual fraction of molecular hydrogen occupying the same volume as propylene oxide is hard to estimate.

## 5. Conclusion

We have presented the first set of collisional rate coefficients for the rotational excitation of propylene oxide by para- $\text{H}_2$  in the temperature range 5–30 K. The scattering calculations were performed on the  $\text{CH}_3\text{CHCH}_2\text{O}$ –He PES of Faure et al. (2019) with the Hibridon code. Collisional and radiative Einstein coefficients were then combined in a non-LTE radiative transfer model in order to reproduce the three absorption lines of propylene oxide detected by McGuire et al. (2016). Our best-fit model suggests that these transitions sample a cold ( $T_{\text{kin}} \sim 10$  K), translucent ( $n_{\text{H}} \sim 2 \times 10^3 \text{ cm}^{-3}$ ), and extended region surrounding Sgr B2(N). Such low densities combined with the relatively strong and extended continuum background toward Sgr B2(N) can successfully explain many of the observed absorption spectra of COMs. On the other hand, weak masers, as studied by Faure et al. (2014) for  $\text{HCOOCH}_3$  and Faure et al. (2018) for  $\text{CH}_2\text{NH}$ , probe a region with larger density  $n_{\text{H}} \sim 10^4 \text{ cm}^{-3}$ .

We have derived a column density for propylene oxide of  $\sim 3 \times 10^{12} \text{ cm}^{-2}$ , in good agreement with previous estimates. This value is a factor of  $\sim 10$ –100 lower than the column densities estimated by McGuire et al. (2016) for the more stable isomers propanal and acetone in the same source. The relative column densities of the three  $\text{C}_3\text{H}_6\text{O}$  isomers should provide another strong constraint on chemical models, but non-LTE calculations are necessary to model propanal and acetone observations, which in turn requires the knowledge of collisional coefficients for these two species.

The constraints and accuracy of the physical parameters predicted by our non-LTE calculations were, in part, determined by the available collisional data and the small number of propylene oxide lines detected in Sgr B2(N). Our model does not predict additional detectable lines toward Sgr B2(N) (except possibly at 15.8 GHz), but it was not possible to explore kinetic temperatures above 30 K. In this context, we note the recent experimental work by Stahl et al. (2021) that should help to assign rotational transitions in the first excited torsional state  $\nu_{24}$  of propylene oxide. Such transitions could be particularly relevant for the detection of propylene oxide in warm,  $T_{\text{kin}} > 100$  K, sources. This will require extension of the present work to include the methyl torsion of propylene oxide, a great challenge for theory.

Finally, in the absence of high-precision polarization measurements, it is currently not possible to distinguish enantiomers in the ISM. The accurate column density and the physical conditions extracted from our non-LTE model,

however, provide important constraints to elucidate the formation pathways to propylene oxide in Sgr B2(N) and therefore to assess the relevance of the various mechanisms able to produce a primordial *ee* in molecular clouds.

This work made use of GBT data from project AGBT07A\_051. The National Radio Astronomy Observatory is a facility of the National Science Foundation operated under cooperative agreement by Associated Universities, Inc. The Green Bank Observatory is a facility of the National Science Foundation operated under cooperative agreement by Associated Universities, Inc. This work has been supported by the French INSU/CNRS Program “Physique et Chimie du Milieu Interstellaire” (PCMI). K.D. acknowledges support by the ERASMUS+ program from European Commission. A.F. and K.D. thank Carlos Pérez del Valle and Rafal Szabla for useful discussions. R.D. and E.Q.-S. are supported by the U.S. Department of Energy (Award DE-SC0019740). Finally, we thank our two referees for their very constructive comments, which have improved the paper. In particular, we thank an anonymous referee for providing the extensive line list of rotational transitions in propylene oxide and the computed radiative data for this molecule using the spectroscopic constants of Creswell & Schwendeman (1977).

### ORCID iDs

Karlis Dzenis  <https://orcid.org/0000-0002-8068-1701>  
 Alexandre Faure  <https://orcid.org/0000-0001-7199-2535>  
 B. A. McGuire  <https://orcid.org/0000-0003-1254-4817>  
 A. J. Remijan  <https://orcid.org/0000-0001-9479-9287>  
 P. J. Dagdigan  <https://orcid.org/0000-0002-6378-221X>  
 F. Lique  <https://orcid.org/0000-0002-0664-2536>

### References

Agúndez, M., Marcelino, N., Tercero, B., et al. 2021, *A&A*, **649**, L4  
 Alexander, M. H., & Manolopoulos, D. E. 1987, *JChPh*, **86**, 2044  
 Alexander, M. H., Manolopoulos, D. E., Werner, H.-J., et al. 2021, HIBRIDON is a package of programs for the time-independent quantum treatment of inelastic collisions and photodissociation, <http://www2.chem.umd.edu/groups/alexander/hibridon>  
 Bacmann, A., Taquet, V., Faure, A., Kahane, C., & Ceccarelli, C. 2012, *A&A*, **541**, L12  
 Bailey, J., Chrysostomou, A., Hough, J. H., et al. 1998, *Sci*, **281**, 672

Balucani, N., Skouteris, D., Ceccarelli, C., et al. 2018, *MolAs*, **13**, 30  
 Bergantini, A., Abplanalp, M. J., Pokhilko, P., et al. 2018, *ApJ*, **860**, 108  
 Bodo, E., Bovolenta, G., Simha, C., & Spezia, R. 2019, *Theor. Chem. Acc.*, **138**, 97  
 Corby, J. 2016, PhD thesis, Univ. of Virginia  
 Corby, J. F., Jones, P. A., Cunningham, M. R., et al. 2015, *MNRAS*, **452**, 3969  
 Creswell, R. A., & Schwendeman, R. H. 1977, *J. Mol. Spectr.*, **64**, 295  
 Cunningham, M. R., Jones, P. A., Godfrey, P. D., et al. 2007, *MNRAS*, **376**, 1201  
 Das, A., Gorai, P., & Chakrabarti, S. K. 2019, *A&A*, **628**, A73  
 Dreiling, J. M., & Gay, T. J. 2014, *PhRvL*, **113**, 118103  
 Faure, A., Dagdigan, P. J., Rist, C., et al. 2019, *ESC*, **3**, 964  
 Faure, A., Hily-Blant, P., Le Gal, R., Rist, C., & Pineau des Forêts, G. 2013, *ApJL*, **770**, L2  
 Faure, A., Jankowski, P., Stoecklin, T., & Szalewicz, K. 2016, *NatSR*, **6**, 28449  
 Faure, A., Lique, F., & Remijan, A. J. 2018, *J. Phys. Chem. Lett.*, **9**, 3199  
 Faure, A., Remijan, A. J., Szalewicz, K., & Wiesenfeld, L. 2014, *ApJ*, **783**, 72  
 Gal, J. 2011, *Chirality*, **23**, 1  
 Garrison, B. J., Lester, W. A., & Miller, W. H. 1976, *JChPh*, **65**, 2193  
 Glavin, D. P., & Dworkin, J. P. 2009, *PNAS*, **106**, 5487  
 Gratier, P., Pety, J., Guzmán, V., et al. 2013, *A&A*, **557**, A101  
 Herbst, E., & van Dishoeck, E. F. 2009, *ARA&A*, **47**, 427  
 Herschbach, D. R., & Swalen, J. D. 1958, *JChPh*, **29**, 761  
 Hollis, J. M., Jewell, P. R., Remijan, A. J., & Lovas, F. J. 2007, *ApJL*, **660**, L125  
 Hudson, R. L., Loeffler, M. J., & Yocum, K. M. 2017, *ApJ*, **835**, 225  
 Joyce, G. F., Schwartz, A. W., Miller, S. L., & Orgel, L. E. 1987, *PNAS*, **84**, 4398  
 McGuire, B. A., Carroll, P. B., Loomis, R. A., et al. 2016, *Sci*, **352**, 1449  
 Modica, P., Meinert, C., de Marcellus, P., et al. 2014, *ApJ*, **788**, 79  
 Müller, H. S., Schlöder, F., Stutzki, J., & Winnewisser, G. 2005, *JMoSt*, **742**, 215  
 Palazzetti, F., Cappelletti, D., Coletti, C., Falcinelli, S., & Pirani, F. 2021, *J. Chem. Phys.*, **155**, 234301  
 Paulive, A., Shingledecker, C. N., & Herbst, E. 2021, *MNRAS*, **500**, 3414  
 Pizzarello, S., & Yarnes, C. T. 2018, *E&PSL*, **496**, 198  
 Remijan, A. J., Hollis, J. M., Lovas, F. J., et al. 2008, *ApJL*, **675**, L85  
 Requena-Torres, M. A., Martín-Pintado, J., Rodríguez-Franco, A., et al. 2006, *A&A*, **455**, 971  
 Rivilla, V. M., Martín-Pintado, J., Jiménez-Serra, I., et al. 2020, *ApJL*, **899**, L28  
 Schmiedeke, A., Schilke, P., Möller, T., et al. 2016, *A&A*, **588**, A143  
 Šebestík, J., & Bouř, P. 2011, *J. Phys. Chem. Lett.*, **2**, 498  
 Stahl, P., Arenas, B. E., Zingsheim, O., et al. 2021, *JMoSp*, **378**, 111445  
 Thiel, V., Belloche, A., Menten, K. M., et al. 2019, *A&A*, **623**, A68  
 Thiel, V., Belloche, A., Menten, K. M., Garrod, R. T., & Müller, H. S. P. 2017, *A&A*, **605**, L6  
 van der Tak, F. F. S., Black, J. H., Schöier, F. L., Jansen, D. J., & van Dishoeck, E. F. 2007, *A&A*, **468**, 627  
 Wang, Y., Du, F., Semenov, D., Wang, H., & Li, J. 2021, *A&A*, **648**, A72  
 Wernli, M., Wiesenfeld, L., Faure, A., & Valiron, P. 2007a, *A&A*, **464**, 1147  
 Wernli, M., Wiesenfeld, L., Faure, A., & Valiron, P. 2007b, *A&A*, **475**, 391